



# High pressure effects on the iron–iron oxide and nickel–nickel oxide oxygen fugacity buffers

Andrew J. Campbell<sup>a,\*</sup>, Lisa Danielson<sup>b</sup>, Kevin Righter<sup>b</sup>, Christopher T. Seagle<sup>c</sup>, Yanbin Wang<sup>d</sup>, Vitali B. Prakapenka<sup>d</sup>

<sup>a</sup> Department of Geology, University of Maryland, College Park, MD 20742, USA

<sup>b</sup> Johnson Space Center, NASA, Houston, TX 77058, USA

<sup>c</sup> Department of the Geophysical Sciences, University of Chicago, Chicago, IL 60637, USA

<sup>d</sup> Consortium for Advanced Radiation Sources, The University of Chicago, Argonne, IL 60439, USA

## ARTICLE INFO

### Article history:

Received 27 April 2009

Received in revised form 13 July 2009

Accepted 16 July 2009

Available online 25 August 2009

Editor: L. Stixrude

### Keywords:

oxygen fugacity  
high pressure  
equations of state

## ABSTRACT

The chemical potential of oxygen in natural and experimental samples is commonly reported relative to a specific oxygen fugacity ( $fO_2$ ) buffer. These buffers are precisely known at 1 bar, but under high pressures corresponding to the conditions of the deep Earth, oxygen fugacity buffers are poorly calibrated. Reference (1 bar)  $fO_2$  buffers can be integrated to high pressure conditions by integrating the difference in volume between the solid phases, provided that their equations of state are known. In this work, the equations of state and volume difference between the metal–oxide pairs Fe–FeO and Ni–NiO were measured using synchrotron X-ray diffraction in a multi-anvil press and laser heated diamond anvil cells. The results were used to construct high pressure  $fO_2$  buffer curves for these systems. The difference between the Fe–FeO and Ni–NiO buffers is observed to decrease significantly, by several log units, over 80 GPa. The results can be used to improve interpretation of high pressure experiments, specifically Fe–Ni exchange between metallic and oxide phases.

© 2009 Elsevier B.V. All rights reserved.

## 1. Introduction

The chemical potential of oxygen is frequently as important as temperature or pressure in controlling the chemical and physical behavior of minerals. Variations in the oxygen potential can cause insulator–metal transformations, for example, or drive large changes in diffusion rates and rheological properties through its control over vacancy populations. Perhaps most important to geochemical consideration, the chemical potential of oxygen can have great effect on elemental partitioning between coexisting phases, particularly when the chemical exchange involves a redox reaction.

In high pressure, high temperature geochemistry experiments, the oxygen fugacity ( $fO_2$ ) is frequently set by, or determined in relation to, a metal–oxide  $fO_2$  buffer (e.g., Fe–FeO, Ni–NiO, Re–ReO<sub>2</sub>) (Dobson and Brodholt, 1999; Rubie, 1999). To compare the experimental results to one another, it is important to know how these buffers change with pressure; otherwise the redox dependence determined by comparison of differently-buffered experiments will be systematically in error. For example, high pressure metal–silicate reactions have been extensively studied using multi-anvil apparatus (e.g., Thibault and Walter, 1995; Li and Agee, 1996; Righter et al., 1997;

Ohtani et al., 1997; Walter et al., 2000; Li and Agee, 2001; Righter, 2003; Wade and Wood, 2005; Corgne et al., 2008; Kegler et al., 2008), and the various systems used as reference buffers in those experiments are imperfectly calibrated against one another at high pressures. Moreover, recent improvements in sample preparation techniques and microanalytical tools have turned the diamond anvil cell into a petrological tool, used to study phase relations and elemental partitioning between phases in recovered high- $P,T$  samples (e.g., Irifune et al., 2005; Takafuji et al., 2005; Auzende et al., 2008; Ricolleau et al., 2008; Sinmyo et al., 2008). As diamond cell technology continues to advance, with improved methods for microanalysis of chemical distributions in the high pressure samples, the chemical activity of oxygen will become an increasingly important factor for interpretation of the experimental results, comparable to the important role  $fO_2$  control plays in lower pressure petrological studies. Likewise, increasingly sophisticated computer simulations of chemical reactions at high pressure can be expected to advance into high pressure petrological studies. The activity of oxygen in these simulations can be varied by adjusting the number of oxygen atoms in the system (e.g., Zhang and Oganov, 2006). Placing these new experimental and computational results in a thermodynamic framework including oxygen fugacity will greatly facilitate the understanding of the results, and also permit separate experiments to be more usefully compared to one another.

\* Corresponding author. Tel.: +1 301 405 4086; fax: +1 301 314 9661.  
E-mail address: [ajc@umd.edu](mailto:ajc@umd.edu) (A.J. Campbell).

Oxygen fugacity ( $fO_2$ ) is a proxy for the chemical activity of oxygen ( $a_{O_2}$ ) in a system. For the general metal–oxide equilibrium reaction



the  $fO_2$  is related to the Gibbs energies ( $G$ ) by

$$\frac{x}{2} RT \ln fO_2 = G(MO_x) - G(M) = \Delta G \quad (2)$$

where  $\Delta G$  is the difference in Gibbs energy between the oxide ( $MO_x$ ) and metal ( $M$ ) phases. The pressure effect on the  $fO_2$  buffer is thus related to the change in  $\Delta G$  with pressure. Along each isotherm,  $\partial G / \partial P|_T = V$ , so the effect of pressure on  $fO_2$  depends on the volume difference ( $\Delta V$ ) between oxide and metal:

$$\partial(\ln fO_2) / \partial P|_T = (2 / xRT) \Delta V \quad (3)$$

One can construct high pressure  $fO_2$  buffer curves by integrating Eq. (3) isothermally to a specified pressure, using appropriate equation of state data for each phase buffering the oxygen activity (metal and oxide, in the example here). However, some of the relevant equations of state are poorly known even for commonly used buffer materials.

In this study we present high pressure, high temperature oxygen fugacity curves for the Fe–FeO and Ni–NiO reactions. These buffers were chosen for their great importance to deep Earth geochemical studies. The Fe–FeO reaction dominates the redox conditions of the deep Earth because of the association of the metallic core with a mantle containing significant amounts of oxidized iron. Consequently, many high pressure geochemical experiments are performed under conditions close to this buffer. Likewise, the Ni–NiO buffer is widely used to produce more oxidizing conditions in geochemical or petrological experiments. Of particular importance are studies of metal–silicate partitioning, that are carried out to understand the observed budget of moderately and highly siderophile elements in the mantle. Nickel is a key trace element in these studies, because its well-constrained mantle abundance (McDonough and Sun, 1995) is thought to be a consequence of metal–silicate equilibration during core–mantle segregation in the early Earth (Li and Agee, 1996; Ohtani et al., 1997).

To determine these high pressure buffer curves, we propagate the well-established 1 bar buffers to high pressure using Eq. (3). The high- $P,T$  values of  $\Delta V$  that we use are determined experimentally by in situ X-ray diffraction measurements of the metal–oxide pairs coexisting under identical high- $P,T$  conditions. Comparing  $V$  between two independently measured equations of state compounds the errors associated with them. Therefore, we measured coexisting metal–oxide buffer pairs simultaneously, which minimizes systematic biases that might appear between separate studies and improves the precision of the  $\Delta V$  data used to determine the high pressure  $fO_2$  buffers. A wide range of  $P,T$  conditions, exceeding 65 GPa and 2400 K, was covered by the use of two different high pressure technologies, the multi-anvil press (MAP) and the laser-heated diamond anvil cell (DAC).

## 2. Experimental

### 2.1. Multi-anvil press

The multi-anvil press (MAP) samples were prepared in the Johnson Space Center high pressure laboratory. The sample materials were mixtures of 1:1 by weight of Ni:NiO or Fe:Fe<sub>1-x</sub>O, all obtained from Alfa Aesar. These were then mixed with 50% NaCl by weight, which acted as an internal pressure standard and also helped to distribute the sample material, inhibiting excessive grain growth that would deleteriously affect the X-ray diffraction measurements. Each high- $P,T$  run included either Ni:NiO or Fe:Fe<sub>1-x</sub>O, not both. The

sample mixtures were loaded into a boron nitride capsule and set into either a 14/8 or 10/5 octahedral MAP assembly. These octahedral assemblies were developed by the COMPRES multi-anvil assembly initiative, and were designed specifically for use in synchrotron-based multi-anvil experiments (Leinenweber et al., 2006). The 14/8 G2 in situ assembly is a graphite box furnace with a forsterite insulating sleeve. The heater and sleeve were X-ray transparent, easily permitting X-ray diffraction measurements, but heating was limited to <1000 °C, <13 GPa to avoid graphite-to-diamond conversion. The 10/5 in situ assembly expanded the pressure range achievable, and temperature was limited by melting of the NaCl. X-ray transmission through the Re foil heaters was allowed by fabricated small slits aligned with Al<sub>2</sub>O<sub>3</sub> windows in the LaCrO<sub>3</sub> insulating sleeve. This allowed X-ray transmission through the sample chamber, but introduced Al<sub>2</sub>O<sub>3</sub> diffraction peaks in the measured spectrum.

The octahedral assemblies were loaded into the 1000-ton multi-anvil press at beamline 13-ID-D of the GSECARS sector of the Advanced Photon Source (Uchida et al., 2002). The samples were oven dried before loading them into the press. They were then pressurized for in situ, high- $P,T$  X-ray diffraction using synchrotron radiation. The X-ray source was a white beam, collimated to approximately 100  $\mu\text{m} \times 100 \mu\text{m}$  using two pairs of WC slits. Diffracted X-rays were measured using a Ge solid state energy dispersive detector at a fixed angle of 6.1°. The detector had 4000 channels, and the exposure times were typically 5 min.

In most experiments, the sample was pressurized to its maximum pressure (~12 GPa in these experiments) before any equation of state data were collected. Then the sample was heated to the maximum target temperature, which caused some reduction of pressure. Pressure–volume–temperature ( $P$ – $V$ – $T$ ) diffraction data were collected on cooling cycles, when non-hydrostatic stresses had been relaxed. After each cooling cycle, the press load was reduced, the sample was heated, and data collection resumed on the next cooling cycle. Data were collected in temperature intervals of 200 °C.

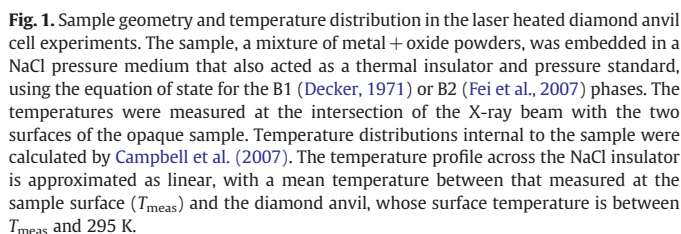
The detector angle was calibrated using the zero pressure lattice spacing of NaCl ( $a = 5.6402 \text{ \AA}$ , JCPDS card #05-0628), measured from each sample before initial compression. The recorded X-ray diffraction patterns were analyzed using PeakFit (Systat Software, Inc.); this involved background subtraction and peak fitting, including deconvolution of overlapping peaks. In addition to the sample materials, the NaCl pressure standard, and the Al<sub>2</sub>O<sub>3</sub> windows, both diffraction and X-ray fluorescence from the Re foil heaters were sometimes detected. Lattice parameters were calculated from at least 3 lines for all samples of hexagonal symmetry, and at least 2 lines for isometric samples. Uncertainties on the lattice parameters reflect standard deviations from multiple diffraction peaks. Pressures were determined from the Decker equation of state for the B1 phase of NaCl (Decker, 1971).

Stoichiometric FeO is only stable at high  $P$  and  $T$ ; at lower pressures and temperatures non-stoichiometric wüstite is observed, with variable composition, even when coexisting at equilibrium with Fe metal (Stølen and Grønvold, 1996). We used  $\Delta V_{\text{w}}$  data only from the  $P$ – $T$  range in which stoichiometric FeO coexisted with fcc-Fe according to the model B phase diagram of Stølen and Grønvold (1996); their model B was chosen because the bulk modulus values in that model are consistent with those in Fei (1996) and Haavik et al. (2000), and also the bulk modulus determined in the present study. Stølen and Grønvold's (1996) result is that FeO coexisting with Fe metal is stoichiometric above 5 GPa at 900 K, with a slope  $< -120 \text{ K/GPa}$ .

### 2.2. Laser-heated diamond anvil cell

The diamond anvil cell (DAC) samples were prepared in the University of Maryland Laboratory for Mineral Physics. The sample materials were mixtures of either Ni–NiO or Fe–Fe<sub>1-x</sub>O, using similar materials as were used in the MAP experiments, and were finely ground to ~1  $\mu\text{m}$  grain size in an agate mortar. These mixtures were

The temperature distribution in the sample and the NaCl insulator during laser heating is schematically illustrated in Fig. 1. The distribution within the sample was calculated from the diffusion equation, with a gaussian distribution imposed on the sample surfaces as boundary conditions (Campbell et al., 2007). The temperature gradient across the NaCl layers, in the region probed by the X-ray beam, lies between  $T_{\text{meas}}$  at the sample surface to  $T_{\text{anvil}}$  at the anvil surface, and the average temperature over which X-rays are diffracted from the pressure medium,  $T_{\text{NaCl}}$ , is  $(T_{\text{meas}} - T_{\text{anvil}})/2$ . Departures from linearity of this gradient may result from several sources,



In Table S2, the structure of the Fe phase (fcc or hcp) is also indicated. Only those phases that were stable under the indicated  $P,T$



conditions (Shen et al., 1998) are included; occasionally a metastable phase of Fe was observed, but these molar volumes are not reported. All reported data have FeO in the B1 structure. The high pressure rhombohedral phase of wüstite (Fei and Mao, 1994) exists only at temperatures lower than those needed for our intended application of constructing high pressure  $fO_2$  buffers. At high pressures and high temperatures a B8-type phase of  $Fe_{1-x}O$  has been reported (Fei and Mao, 1994; Murakami et al., 2004), but this phase was not seen in our results nor in those of Seagle et al. (2008). We speculate that this could be because of the stoichiometry of our FeO phase ( $x=0$ ). In addition to the data listed in Table S2, our analysis includes the  $P$ – $V$ – $T$  data from Seagle et al. (2008), who used virtually identical experimental methods in their DAC study of the Fe–FeO system. The molar volumes of Fe and FeO are plotted in Fig. 2, and the corresponding  $\Delta V_{IW}$  is plotted in Fig. 4. Although MAP experiments can be performed at a predetermined temperature, controlled by feedback from the thermocouple, laser-heated DAC experiments do not so easily permit a tightly specified temperature, and the temperature values are usually determined after the fact. For this reason, the data in the figures are coded by temperature range, rather than plotted as sets of isothermal data.

In Table S3, all of the Ni data refer to the fcc structure, and all of the NiO data refer to the B1 structure. No other phases were observed. The molar volumes of Ni and NiO at high pressure and temperature are plotted in Fig. 3, and the  $\Delta V_{NNO}$  values are plotted in Fig. 4.

## 4. Discussion

### 4.1. Equations of state and $\Delta V_{ox-met}$ at high pressures and temperatures

In many geophysical applications, the difference in molar volume (or density) between phases is more important than the absolute volumes (or densities) of those phases. The application that we intend for the present data, calculating the thermodynamics of chemical equilibria at high pressure, is one example. In these cases, there are significant advantages to measuring the two phases simultaneously,

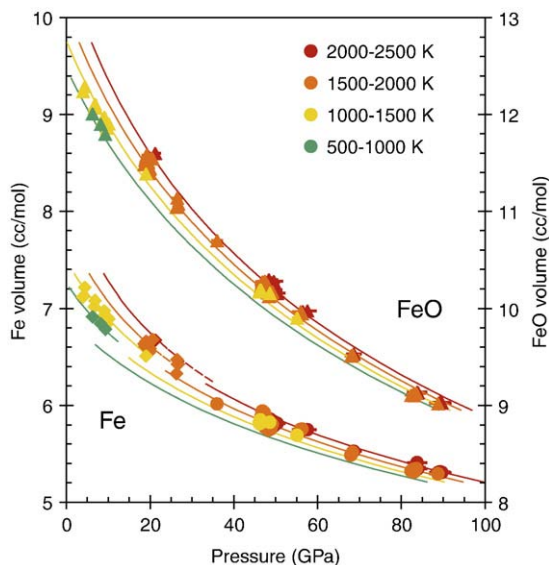


**Fig. 2.** Equation of state data for Fe and FeO. Data below 15 GPa were obtained by MAP; higher pressure data were obtained by DAC (this study and from Seagle et al. (2008)). Squares: fcc-Fe; circles: hcp-Fe; triangles: FeO. Only the B1 phase of FeO was observed in coexistence with Fe at high pressure and temperature. The data were obtained only at  $P$ ,  $T$  conditions sufficiently high to ensure stoichiometric  $Fe_{1.000}O$  (Stølen and Grønvold, 1996). Data are color coded to indicate temperature. Shown for comparison are the Dewaele et al. (2006) equation of state for hcp-Fe and equations of state from Table 1 at various temperatures. Each colored curve represents the midpoint of the temperature range indicated. (For interpretation of the references to color in this figure legend, the reader is referred to the web version of this article.)

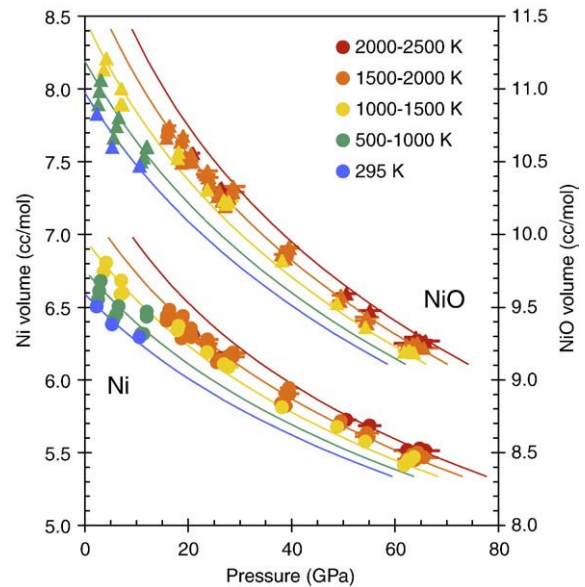


**Fig. 3.** Equation of state data for Ni and NiO. Data below 15 GPa were obtained by MAP; higher pressure data were obtained by DAC. Circles: Ni; triangles: NiO. Data are color coded to indicate temperature. A Mie–Grüneisen equation of state is fit to the data at different temperatures as shown. Each colored curve represents the midpoint of the temperature range indicated. (For interpretation of the references to color in this figure legend, the reader is referred to the web version of this article.)

under identical  $P$ ,  $T$  conditions, rather than comparing two independently determined equations of state to one another. Equation of state studies can suffer from systematic biases resulting from their experimental procedures. For example, pressure standards are not all perfectly consistent with one another. Although there is ongoing work in improving this situation by comparing pressure standards to one another (Fei et al., 2007; Dorogokupets and Oganov, 2007; Dewaele et al., 2008), there is already a voluminous literature in which various, inconsistent pressure scales were used. When it is critical to compare the volumes of two phases directly, a better strategy is to measure them simultaneously to avoid problems related to inconsistency in pressure standards. Furthermore, holding the two phases together under high  $P$ ,  $T$  conditions allows them to reach chemical equilibrium with one another. This is a very important advantage when there is a new phase, or new stoichiometry, that

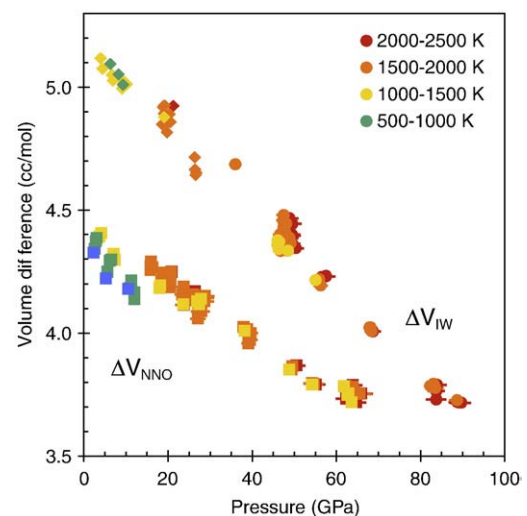


**Fig. 4.** Volume differences between coexisting oxide and metal at high pressures and temperatures, from the data in Figs. 2 and 3. Diamonds: FeO–fcc Fe; circles: FeO–hcp Fe; squares: NiO–Ni.

exists in the system only at high  $P$  and  $T$ , and not under ambient conditions. This is the case in the Fe–FeO system. At 1 bar the stoichiometric  $\text{Fe}_{1.00}\text{O}$  phase is not stable, but at high- $P,T$  conditions non-stoichiometric wüstite can react with metallic Fe to form  $\text{Fe}_{1.00}\text{O}$  (Stölen and Grønvold, 1996); this fact was exploited in the present study. For all of these reasons, we chose to measure  $\Delta V_{\text{ox-met}}$  in the Fe–FeO and Ni–NiO systems by simultaneous measurement of the molar volumes of metal and coexisting oxide at high pressures and temperatures. This strategy improves the precision to which the  $\Delta V$  values are determined, thereby improving the calculation of oxygen fugacity buffers at high pressure.

High pressure, high temperature equations of state were derived for each phase by fits to the combined MAP and DAC data. A Mie–Grüneisen equation of state was used,

$$P = P_{295}(V) + (\gamma/V)[E(\theta_D, T) - E_{295}(\theta_D, 295)] \quad (5)$$

with the 295 K isotherm ( $P_{295}$ ) described by a Birch–Murnaghan equation and the thermal pressure term based on a Debye model of vibrational energy ( $E$ ), with Grüneisen parameter  $\gamma = \gamma_0(V/V_0)^q$  and Debye temperature  $\theta_D = \theta_0(V/V_0)^{-\gamma}$ . Although this formalism does not explicitly include parameters for anharmonic or electronic contributions, it is identical to that used to describe the NaCl–B2, Pt, Au, and Ne equations of state by Fei et al. (2007). Parameters used in the least-squares fits to the equation of state data are presented in Table 1. We do not offer an alternative set of equation of state parameters for hcp-Fe, because no fit to our data was superior to the Dewaele et al. (2006) equation, so we used it in our analysis instead. (The agreement between our data and the Dewaele et al. (2006) equation for hcp-Fe is further evidence that the NaCl pressure medium can act as an effective pressure standard, as described above, during high temperature laser heating experiments when stress gradients have been relaxed.)

By combining data from the two different experimental methods (MAP and DAC), we were able to investigate a more complete range of pressures and temperatures than either method can cover alone. In principle this approach provides a more robust equation of state, but one potential concern is that two different pressure standards were used among the measurements (NaCl–B1 for low pressures; NaCl–B2 for high pressures). Residuals from the fitted equations of state in Table 1 do not reveal systematic biases between the two methods or between the two pressure calibrations. However, this may simply be a consequence of there being little overlap in  $P,T$  conditions covered by the two methods, and larger uncertainties related to the thermal gradient across the NaCl standard in the laser heated DAC experiments. Overlapping measurements at low pressure and high temperature were precluded by melting of the NaCl standard, so direct comparisons cannot easily be made between the complementary but separate data sets. The present results therefore rely on the accuracy

of the widely used equation of state of NaCl–B1 (Decker, 1971) and the fact that the NaCl–B2 equation of state has been cross-calibrated against multiple other  $P$ – $V$ – $T$  standards (Fei et al., 2007).

Volume differences (Fig. 4) between NiO and Ni,  $\Delta V_{\text{NNO}}$ , and between FeO and Fe,  $\Delta V_{\text{IW}}$ , are also included in Tables S2 and S3. There is no functional form that one should expect the  $\Delta V$ – $P$ – $T$  data to follow, so the  $\Delta V$  data were not fit to an equation. Instead, in the calculations below the  $\Delta V$  values were determined numerically from the fitted equations of state given in Table 1; the volumes at each pressure and temperature were determined iteratively to a precision of  $<10^{-4}$  GPa in pressure.

#### 4.2. Calculation of high pressure buffers

In this section we use the analyses of  $\Delta V$ – $P$ – $T$  data in Section 4.1 to calculate the NNO and IW (strictly, Fe–FeO) oxygen fugacity buffer curves at high pressures. The calculations proceed by integration of Eq. (3), with  $x = 1$  for both FeO and NiO:

$$\log f_{\text{O}_2} = \log f_{\text{O}_2}(1\text{bar}) + (0.8686/RT) \int \Delta V dP \quad (6)$$

where the conversion from  $\ln$  to  $\log_{10}$  was made. The 1 bar  $f_{\text{O}_2}$  buffers were calculated using the thermodynamic data in Chase (1998) for stoichiometric FeO and Knacke et al. (1991) for NiO. Only  $\Delta G$  data below the melting points were used, but extrapolations of these data to higher temperatures was made to facilitate analysis of high- $P,T$  data. High pressure  $f_{\text{O}_2}$  buffer curves were calculated along a set of isotherms from 1000 K to 2600 K, in 100 K intervals. Integration of  $\Delta V dP$  for each metal–oxide system utilized the  $\Delta V$  values calculated from the equations of state above. For the IW system, integration proceeded using the fcc–Fe data up to the fcc–hcp transition pressure (Shen et al., 1998) at each temperature; above this transition pressure the  $\Delta V_{\text{IW}}$  data for hcp–Fe were used in the integration.

The IW buffer at 1 bar and at high pressures is shown in Fig. 5a. Tabulated values at smaller pressure increments are presented in Table S4 in the Supplementary Material. There are two primary effects of pressure on the IW  $f_{\text{O}_2}$  curve. The first is that the absolute  $f_{\text{O}_2}$  values increase with pressure at each temperature. The second effect is that the slope  $\partial(\ln f_{\text{O}_2})/\partial T|_P$  decreases with pressure, eventually becoming a slope of approximately zero at 60 GPa, and negative at higher pressures. At pressures higher than 60 GPa, the slope of the oxygen fugacity curve with  $T$  is negative, so at a fixed  $f_{\text{O}_2}$ , increasing temperature drives Fe toward oxidation. This is the opposite of the behavior familiar at 1 bar or other low-pressure conditions, and is not specific to the Fe–FeO buffer. Any oxygen fugacity buffer will eventually obtain a negative  $\partial(\ln f_{\text{O}_2})/\partial T|_P$  slope at high pressure, because the pressure derivative  $\partial(\ln f_{\text{O}_2})/\partial P|_T$  is greater at low temperatures than it is at high temperatures, following Eq. (3).

The analogous calculation for the NNO buffer curves at 1 bar and at high pressures is illustrated in Fig. 5b (calculated values in Table S5 of Supplementary Material). These curves are always higher than the IW buffer curves at the same pressure, reflecting the higher siderophilicity of Ni relative to Fe. However, the pressure effect on the NNO buffer is not as great as that for the IW buffer, because  $\Delta V_{\text{NNO}}$  is smaller than  $\Delta V_{\text{IW}}$ . Consequently, the difference between the NNO buffer and the IW buffer decreases with pressure. For example, at 1500 K this difference is 4.78  $\log f_{\text{O}_2}$  units at 1 bar but only 2.38  $\log f_{\text{O}_2}$  units at 60 GPa. One way to view this is that Ni becomes less siderophile with increasing pressure.

To illustrate more explicitly how the difference between the buffer curves (NNO–IW) varies with pressure, these values are plotted in Fig. 5c. This figure allows one to quickly evaluate the difference between the buffers at any  $P,T$  condition within the range covered by this study. More precise values can be determined from Tables S4 and S5 in the Supplementary Material, where numerical  $\log f_{\text{O}_2}$  values for

**Table 1**  
Equation of state (Birch–Murnaghan) parameters.

	Fe–fcc	FeO–B1	Ni	NiO
$V_0$ , cm <sup>3</sup> /mol	7.076 <sup>a</sup>	12.256 <sup>b</sup>	6.587 <sup>a</sup>	10.973 <sup>a</sup>
$K$ , GPa	133 ± 3	146.9 ± 1.3	179 ± 3	190 ± 3
$K'$	5 <sup>c</sup>	4 <sup>d</sup>	4.3 ± 0.2	5.4 ± 0.2
$\theta_D$ , K	470 <sup>e</sup>	380 <sup>e</sup>	415 <sup>f</sup>	480 <sup>f</sup>
$\gamma_0$	1.95 ± 0.04	1.42 ± 0.04	2.50 ± 0.06	1.80 ± 0.04
$Q$	1.6 ± 0.6	1.3 ± 0.3	1	1

Entries in italics held fixed in the fit:

<sup>a</sup> JCPDS card files.

<sup>b</sup> McCammon and Liu, 1984.

<sup>c</sup> Funamori et al., 1996.

<sup>d</sup> Fei, 1996.

<sup>e</sup> Chase, 1998.

<sup>f</sup> Knacke et al., 1991.

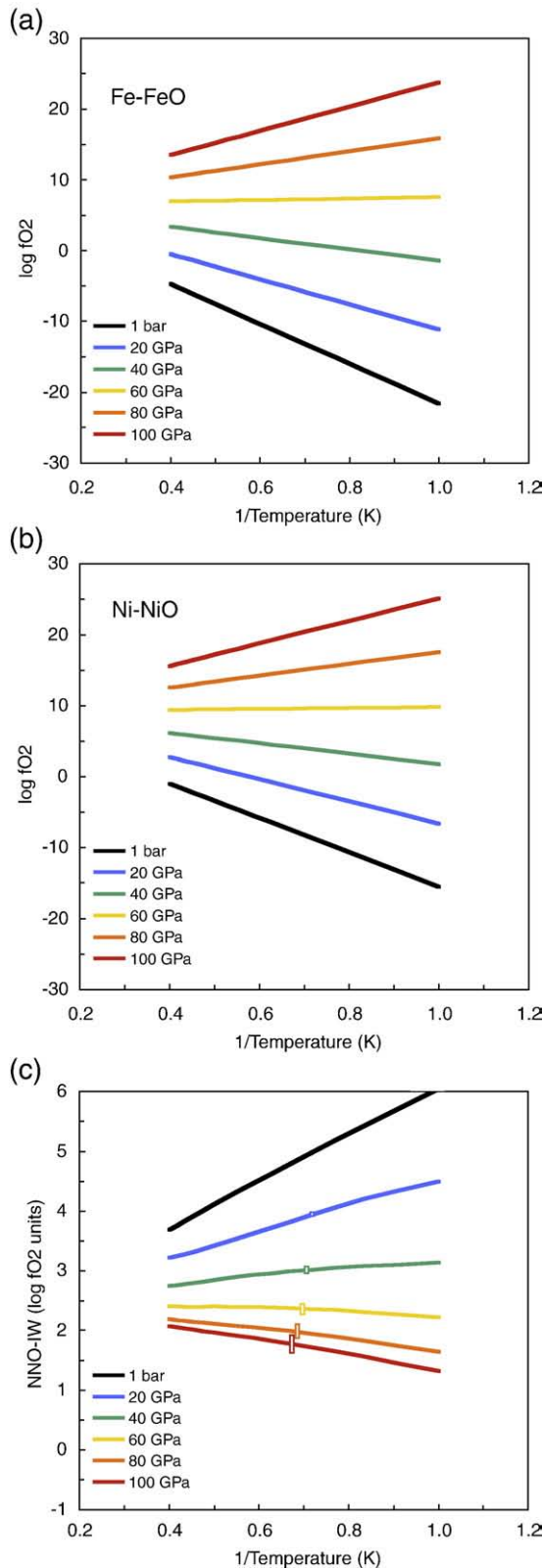


**Fig. 5.** (a) Fe–FeO and (b) Ni–NiO oxygen fugacity buffers, and (c) the difference between them, at various pressures. The 1 bar buffer curves were calculated from Chase (1998) and Knacke et al. (1991), and high pressure curves were calculated from Eq. (6) using fits to the data like those in Figs. 2 and 3. With increasing pressure and temperature, the difference between the Ni–NiO and Fe–FeO buffers decrease, indicating decreasing siderophilicity of Ni. Uncertainties are indicated in (c) by vertical bars.

the IW and NNO oxygen fugacity buffers are listed, and coefficients to a polynomial fit to the  $\log fO_2$  values are also provided. Misfits to the equations of state produce r.m.s. values on  $\Delta V$  of approximately  $0.03 \text{ cm}^3/\text{mol}$  for both buffers; this contributes uncertainty to the calculated buffers that is proportional to  $P/T$ , reaching  $\pm 0.2$  log units at 100 GPa and 1500 K.

Contrary to the low pressure circumstances, the difference between the two buffers has a negative slope above  $\sim 50$  GPa (Fig. 5c). This implies that at high pressures Ni becomes more siderophile with increasing temperature; Kegerl et al. (2008) noted a similar effect in their data regression, but at somewhat lower pressure,  $\sim 30$  GPa.

#### 4.3. Applications

As petrological and geochemical studies extend deeper into the Earth, it is necessary to have a thermodynamic framework in place in which to interpret the data. The present study is a step in this necessary direction, by extending two commonly used buffers to great depths in the Earth and illustrating the pressure-induced changes in the difference between them. One might consider how the Fe–FeO and NNO buffers relate to one another along the pressure–temperature path in the Earth's deep mantle. We show this comparison in Fig. 6, in which the values of these two buffers are shown along a representative geotherm, in this case the Brown and Shankland (1981) model. At 1 bar and 1400 K, the difference between the NNO and Fe–FeO buffers is 5.0 log units. By 670 km (23.8 GPa by PREM (Dziewonski and Anderson, 1981) and 1873 K by Brown and Shankland (1981)), this difference has dropped to 3.4 log units, and at 2000 km depth (86.9 GPa, 2256 K) the difference is only 2.1 log units. This relative change in the metal–oxide buffers should manifest itself in changing chemical behavior of Ni. The oxygen fugacity of the mantle is largely reflected in the redox state of Fe, and there is a body of evidence that much of the mantle is saturated in Fe-rich metal (Frost and McCammon, 2008), so the mantle  $fO_2$  should lie just below the Fe–FeO buffer shown in Fig. 6. The exchange of Fe and Ni between phases will vary with depth according to the variation in differences in buffers shown in the figure. One expects on this basis that Ni will be less strongly siderophile at depth, relative to Fe.

More generally, the pressure dependence on differences in  $fO_2$  buffers can play a role in understanding, from a thermodynamic perspective, why chemical partitioning behavior varies the way it does with pressure. For example, as pressure and temperature increase, the NNO and IW buffer curves converge (Fig. 5c); in essence, Ni becomes less siderophile. Holding other factors (namely activity coefficients) equal, one would then expect that with increasing pressure, the Ni–Fe exchange coefficient between metal and silicate or oxide would decrease. This is in fact observed; partitioning studies between liquid silicate and metal show that  $K_{\text{met/sil}}^{\text{Ni-Fe}}$  decreases with increasing pressure (Thibault and Walter, 1995; Li and Agee, 1996, 2001; Bouhifd and Jephcoat, 2003; Corgne et al., 2008). There is an extensive literature from these experimental studies, principally with the goal of understanding chemical exchange and equilibration between the silicate mantle and the segregating core during early Earth differentiation. Parameterizations in  $P$ ,  $T$ ,  $fO_2$ , and  $nbo/t$  have been crucial to comprehensive understanding of metal/silicate partitioning (Righter, 2003). Evolution of these parameterizations, using more robust thermodynamic treatment of the oxygen fugacity states in the experiments, is a natural way to augment the existing data to improve its accuracy and power of prediction, and also to better guide future experimentation.

Metal silicate partition coefficients ( $D = X^{\text{met}}/X^{\text{sil}}$ ) are commonly parameterized with linear dependence on temperature, pressure, oxygen fugacity, silicate polymerization ( $nbo/t$ ), and/or sulfur ( $X_S$ ) and carbon ( $X_C$ ) content of the metallic melt (e.g., Righter, 2003):

$$\log D = a + bT + c(P/T) + d \log fO_2 + e(nbo/t) + f \log(1 - X_S) + g \log(1 - X_C) \quad (7)$$



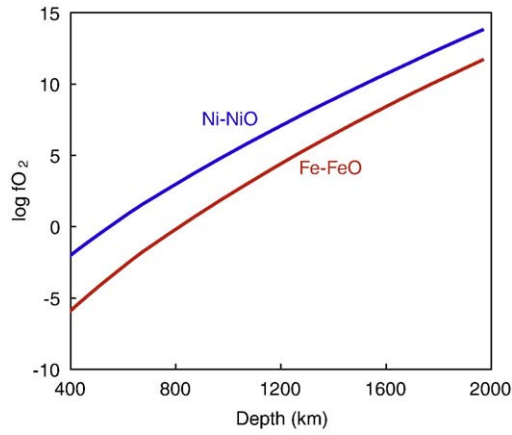


**Fig. 6.** Fe–FeO and Ni–NiO oxygen fugacity buffers along a representative geotherm through the Earth's mantle (Brown and Shankland, 1981; Dziewonski and Anderson, 1981). At 2000 km depth, the pressure and temperature are 86.9 GPa and 2256 K. The difference between the two buffers decreases from 5.0 log units at 1 bar, 1400 K to 2.1 log units at 2000 km depth.

This method has been shown to be effective at describing experimental data over the range of their measurement conditions (Righter, 2003). However, extrapolations must be treated with caution because of the assumed linearity. Here, we recast this equation to permit nonlinear dependence on pressure:

$$\log D = \Delta G^{\text{MMO}} / (RT \ln 10) - \log (\gamma_{\text{M}} / \gamma_{\text{MO}_x}) - x/2 \log f\text{O}_2 \quad (8)$$

where the most of the pressure dependence is in the  $\Delta G^{\text{MMO}}$  term through Eqs. (3) and (6), although there may also be pressure dependence to the activity coefficients,  $\gamma$  (i.e., nonzero mixing volumes). The  $f\text{O}_2$  dependence of metal–silicate partitioning is strong, and it is useful to eliminate it by considering, instead of the partition coefficient, an exchange coefficient,  $K_D$ . For M–Fe exchange:

$$K_D = D(\text{M}) / D(\text{Fe})^x = \left( X_{\text{M}}^{\text{met}} / X_{\text{MO}_x}^{\text{sil}} \right) / \left( X_{\text{Fe}}^{\text{met}} / X_{\text{FeO}}^{\text{sil}} \right)^x \quad (9)$$

$$\log K_D = x/2 \left( \log f\text{O}_2^{\text{MMO}} - \log f\text{O}_2^{\text{IW}} \right) + \log \left( \gamma_{\text{MO}_x}^{\text{sil}} / \gamma_{\text{M}}^{\text{met}} \right) / \left( \gamma_{\text{FeO}}^{\text{sil}} / \gamma_{\text{Fe}}^{\text{met}} \right)^x \quad (10)$$

from Eqs. (2) and (8).

We can use Eq. (10), combined with the high pressure values of  $\log f\text{O}_2^{\text{NNO}} - \log f\text{O}_2^{\text{IW}}$  calculated in the previous section, to predict the pressure dependence of Ni–Fe exchange between metal and silicate. In Fig. 7 the ratio of activity coefficients is chosen to satisfy the low pressure experimental data for  $K_D^{\text{Ni-Fe}}$  between iron-rich metallic melt and mafic silicate melt (Li and Agee, 1996; Ito et al., 1998), and Eq. (10) is applied with our results on the  $f\text{O}_2$  buffers of Ni–NiO and Fe–FeO to predict the pressure dependence of  $K_D^{\text{Ni-Fe}}$ . We use the Li and Agee (1996) and Ito et al. (1998) studies to make this comparison, because in each of these studies the metal and silicate compositions remained nearly constant (although they differ between the two data sets), and both reached fairly high pressure. Two assumptions are made in this calculation. First, it is assumed that the activity coefficients (or at least the ratio of activity coefficients) are constant with pressure. Second, the calculation assumes that the free energy differences between solid and liquid ( $\Delta G_{\text{liquid}}^{\text{MMO}} - \Delta G_{\text{solid}}^{\text{MMO}}$ ) are equal for the Ni–NiO system and the Fe–FeO system. This assumption is necessary because, although our high pressure buffer curves are calculated for the solid metal–oxide systems, experimental studies of metal–silicate partitioning are generally applied to liquid systems, because their principal application is to elemental partitioning in the conditions of a magma ocean during differentiation of the early Earth.

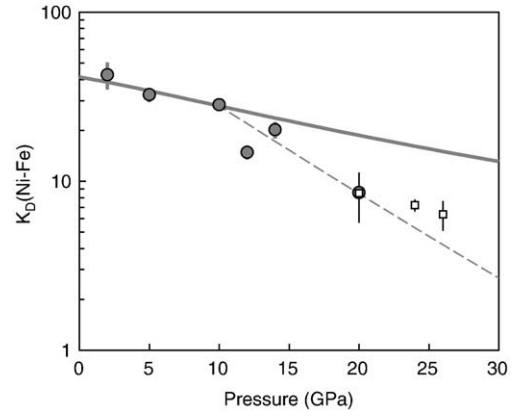


**Fig. 7.** Exchange coefficient ( $K_D$ ) for Ni and Fe between metallic melt and peridotitic silicate at high pressure. Shaded circles: Li and Agee (1996). Open squares: Ito et al. (1998). Solid curve: calculated pressure dependence based on Eq. (10) and experimental equation of state results of this study, assuming that the activity coefficient term in Eq. (10) is constant with pressure. The curve predicts the pressure dependence at low pressures, but above 10 GPa the curve deviates from the data, suggesting nonideal mixing related to changes in the silicate melt structure. Dashed curve: shows the effect of a mixing volume of  $-1.5 \text{ cm}^3/\text{mol}$  applied above 10 GPa.

More rigorously, including the solid-to-liquid terms in deriving Eq. (10) produces:

$$\log K_D = x/2 \left( \log f\text{O}_2^{\text{MMO}} - \log f\text{O}_2^{\text{IW}} \right) + \log \left( \gamma_{\text{MO}_x}^{\text{sil}} / \gamma_{\text{M}}^{\text{met}} \right) / \left( \gamma_{\text{FeO}}^{\text{sil}} / \gamma_{\text{Fe}}^{\text{met}} \right)^x + \left[ \left( \Delta G_{\text{liquid}}^{\text{MMO}} - \Delta G_{\text{solid}}^{\text{MMO}} \right) - x \left( \Delta G_{\text{liquid}}^{\text{IW}} - \Delta G_{\text{solid}}^{\text{IW}} \right) \right] / (RT \ln 10) \quad (11)$$

Eq. (10) is otherwise exact, and deviations away from the prediction of this equation must reflect violations of these two assumptions.

As shown in the figure, Eq. (10) accurately describes the pressure dependence of  $K_D^{\text{Ni-Fe}}$  up to approximately 10–15 GPa, when the activity coefficient ratio is chosen to match the low pressure  $K_D^{\text{Ni-Fe}}$  value. However, at higher pressures the observed metal–silicate partitioning decreases more rapidly than predicted by Eq. (10). One interpretation is that the assumption of constant activity coefficient ratios is violated at high pressure, and the mixing volume of one or more species becomes nonzero at high pressure. This could be related to coordination changes of these transition elements, analogous to those reported in albite melts by Keppler and Rubie (1993), as well as more general structural changes in the silicate melt, that are known to occur in this pressure range (Williams and Jeanloz, 1988; Stebbins et al., 1995; Stixrude and Karki, 2005). Kegler et al. (2008) reported a similar change in the pressure dependence of  $K_D^{\text{Ni-Fe}}$  that they attributed to coordination changes in the silicate melt, although their observed change in  $K_D^{\text{Ni-Fe}}$  behavior occurred at lower pressure ( $\sim 5$  GPa) than seen in Fig. 7. Another interpretation of the departure of the experimental data from the Eq. (10) curve is that the solid-to-liquid correction is significant, and our assumption that the free energy difference ( $\Delta G_{\text{liquid}}^{\text{MMO}} - \Delta G_{\text{solid}}^{\text{MMO}}$ ) is everywhere equal between the Ni–NiO system and the Fe–FeO system is invalid. In this case the pressure dependence of metal–silicate partitioning will require knowledge of the volumes of the melt components, and their pressure dependence. The experimental data on melt components are very limited in pressure, and these have been shown to predict the pressure dependence of  $K_D$  only qualitatively (Courtial et al., 1999).

To illustrate the possible effect of this reformulation of the metal/silicate partitioning data, we postulate the emergence of a nonzero mixing volume for the Ni–Fe exchange reaction above 10 GPa, pursuant to the discussion above. As shown in Fig. 7, a mixing volume of  $-1.5 \text{ cm}^3/\text{mol}$  satisfies the difference between our predicted high pressure behavior for  $K_D^{\text{Ni-Fe}}$  and the results of Li and Agee (1996).

(The suddenness of the mixing volume change shown in Fig. 7 is a simplification.) On the basis of linear extrapolations to their experimental data, Li and Agee (1996) calculated that the Ni and Co abundances in the upper mantle can be explained by partitioning during Earth's core–mantle equilibration in a magma ocean at pressures between 28 and 42 GPa. Our reparameterization of the  $K_D^{\text{Ni-Fe}}$  data, assuming  $\Delta V_{\text{mixing}} = -1.5 \text{ cm}^3/\text{mol}$  (and leaving the Co–Fe exchange parameterization unchanged from Li and Agee (1996)), produces the same degree of partitioning at a lower pressure range, between 24 and 36 GPa. Hence, this change to the parameterization of  $K_D^{\text{Ni-Fe}}$  can impact the inferred pressure of core–mantle equilibration.

The linear pressure dependence of  $\log K_D^{\text{Ni-Fe}}$  that is fitted empirically to high pressure metal–silicate partitioning data (e.g., Li and Agee, 1996; Righter et al., 1997; Righter, 2003; Corgne et al., 2008) data masks two underlying thermodynamic effects, shown in Eqs. (10) and (11). First, the pressure dependence can be understood simply in terms of the volume differences between the Ni–NiO and Fe–FeO buffers, that are components dissolved into the metal and silicate melts. Second, the ratios of activity coefficients relevant to this mixing obtain pressure dependences (nonzero mixing volumes) at pressures above approximately 10–15 GPa (Fig. 7), likely in response to the changing structural coordinations in the silicate melt at this pressure. Over the pressure range obtained by the multi-anvil press data, the pressure dependence of  $K_D$  frequently is well described by a linear term, allowing accurate interpolation and description of the data over this pressure range. However, it is understood that the functional form of the thermodynamic expressions driving this pressure dependence may not be linear, and as illustrated by the example above, with extrapolation to higher pressures and temperatures a linear parameterization will be prone to increasing inaccuracy. It follows that a more thorough analysis of numerous metal–oxide buffers, using their (solid and/or liquid) equations of state at high pressures, offers the prospect of yielding greater resolution of volume vs. structural effects on metal–silicate partitioning of moderately siderophile elements, that will provide more reliable extrapolations to deep Earth conditions to better interpret observed mantle chemistry in terms of the chemical effects of core–mantle segregation.

## 5. Summary

The effect of pressure on oxygen fugacity buffers is calculable to high precision, if a full high pressure, high temperature equation of state is applied for the coexisting species instead of assuming a fixed  $\Delta V$ . Systematic biases between pressure calibrations of equation of state measurements can be minimized by measuring the two (metal and oxide) components together. Furthermore, this approach ensures that the metal and oxide chemically equilibrate with one another, for example driving the iron oxide component to  $\text{Fe}_{1.00}\text{O}$  stoichiometry in the experiments. This method was applied here to the Fe–FeO and Ni–NiO systems, using two complementary experimental methods, a multi-anvil press and diamond anvil cells, for maximum  $P$ – $T$  coverage.

The Ni–NiO and Fe–FeO oxygen fugacity buffers both increase with pressure, but at different rates, such that the difference between them diminishes with pressure. This change in relative  $\log f_{\text{O}_2}$  units is important to consider when comparing results from high pressure experimental runs referenced to the Fe–FeO vs. the Ni–NiO buffers. Along the  $P$ – $T$  path of a nominal mantle geotherm, the difference between the Ni–NiO and Fe–FeO buffers is reduced by nearly three  $\log f_{\text{O}_2}$  units over 2000 km depth in the Earth. This diminishing siderophile nature of Ni is consistent with experimental studies of metal–silicate partitioning of Ni and Fe. The formalism used here allows us to better interpret these data, emphasizing that the pressure effect on  $K_D^{\text{Ni-Fe}}$  has two components, an intrinsic volumetric effect and a possible mixing volume term above 10 to 15 GPa related to structural changes in the silicate melt. With further study covering a variety of moderately siderophile elements, this view of high pressure

geochemical behavior should permit improved extrapolations to the inferred conditions of metal–silicate equilibration during Earth's core formation.

## Acknowledgments

We are grateful to Graham Taylor, Genna Davidson, and Helen Nguyen for their assistance with data processing. Kurt Leinenweber helpfully provided the octahedral assemblies that were specifically designed for synchrotron X-ray diffraction experiments. Comments from two anonymous reviewers guided improvements to the manuscript. This research was partially supported by COMPRES, the Consortium for Materials Properties Research in Earth Sciences under NSF Cooperative Agreement EAR 06-49658. Portions of this work were performed at GeoSoilEnviroCARS (Sector 13), Advanced Photon Source (APS), Argonne National Laboratory. GeoSoilEnviroCARS is supported by the National Science Foundation – Earth Sciences (EAR-0622171), Department of Energy – Geosciences (DE-FG02-94ER14466) and the State of Illinois. Use of the Advanced Photon Source was supported by the U. S. Department of Energy, Office of Science, Office of Basic Energy Sciences, under Contract No. DE-AC02-06CH11357. This work was supported by NSF grant EAR-0635722 (AJC) and an RTOP from the NASA Cosmochemistry program (KR). CTS acknowledges support from DOE–NNSA through the Carnegie/DOE Alliance Center (CDAC).

## Appendix A. Supplementary data

Supplementary data associated with this article can be found, in the online version, at doi:10.1016/j.epsl.2009.07.022.

## References

- Auzende, A.-L., Badro, J., Ryerson, F.J., Weber, P.K., Fallon, S.J., Addad, A., Siebert, J., Fiquet, G., 2008. Element partitioning between magnesium silicate perovskite and ferropericlase: new insights into bulk lower-mantle geochemistry. *Earth Planet. Sci. Lett.* 269, 164–174.
- Bouhifd, M.A., Jephcoat, A.P., 2003. The effect of pressure on partitioning of Ni and Co between silicate and iron-rich metal liquids: a diamond-anvil cell study. *Earth Planet. Sci. Lett.* 209, 245–255.
- Brown, J.M., Shankland, T.J., 1981. Thermodynamic parameters in the Earth as determined from seismic profiles. *Geophys. J. R. Astron. Soc.* 66, 579–596.
- Campbell, A.J., Seagle, C.T., Heinz, D.L., Shen, G., Prakapenka, V.B., 2007. Partial melting in the iron-sulfur system at high pressure: a synchrotron X-ray diffraction study. *Phys. Earth Planet. Inter.* 162, 119–128.
- Chase Jr., M.W., 1998. NIST-JANAF Thermochemical Tables, 4th ed.: J. Phys. Chem. Ref. Data Monograph No. 9. American Institute of Physics.
- Corgne, A., Keshav, S., Wood, B.J., McDonough, W.F., Fei, Y., 2008. Metal–silicate partitioning and constraints on core composition and oxygen fugacity during Earth accretion. *Geochim. Cosmochim. Acta* 72, 574–589.
- Courtial, P., Gottsmann, J., Holzeid, A., Dingwell, D.B., 1999. Partial molar volumes of NiO and CoO liquids: implications for the pressure dependence of metal–silicate partitioning. *Earth Planet. Sci. Lett.* 171, 171–183.
- Decker, D.L., 1971. High pressure equation of state for NaCl, KCl, and CsCl. *J. Appl. Phys.* 42, 3239–3244.
- Dewaele, A., Loubeyre, P., Occelli, F., Mezouar, M., Dorogokupets, P.I., Torrent, M., 2006. Quasihydrostatic equation of state of iron above 2 Mbar. *Phys. Rev. Lett.* 97, 215504.
- Dewaele, A., Torrent, M., Loubeyre, P., Mezouar, M., 2008. Compression curves of transition metals in the Mbar range: experiments and projector augmented-wave calculations. *Phys. Rev. B* 78, 104102.
- Dobson, D.P., Brodholt, J.P., 1999. The pressure medium as a solid-state oxygen buffer. *Geophys. Res. Lett.* 26, 259–262.
- Dorogokupets, P.I., Oganov, A.R., 2007. Ruby, metals, and MgO as alternative pressure scales: a semiempirical description of shockwave, ultrasonic, x-ray, and thermochemical data at high temperatures and pressures. *Phys. Rev. B* 75, 024115.
- Dziewonski, A.M., Anderson, D.L., 1981. Preliminary reference Earth model. *Phys. Earth Planet. Inter.* 25, 297–356.
- Fei, Y., 1996. Crystal chemistry of FeO at high pressure and temperature. In: Dyar, M.D., McCammon, C., Shaefer, M.W. (Eds.), *Mineral Spectroscopy: A Tribute to Roger Burns*. Geochemical Society, Houston, pp. 243–254.
- Fei, Y., Mao, H.-K., 1994. In-situ determination of the NiAs phase of FeO at high pressure and temperature. *Science* 266, 1678–1680.
- Fei, Y., Ricolleau, A., Frank, M., Mibe, K., Shen, G., Prakapenka, V., 2007. Toward an internally consistent pressure scale. *Proc. Natl. Acad. Sci. USA* 104, 9182–9186. doi:10.1073/pnas.0609013104.
- Frost, D.J., McCammon, C.A., 2008. The redox state of Earth's mantle. *Annu. Rev. Earth Planet. Sci.* 36, 389–420.



- Funamori, N., Yagi, T., Uchida, T., 1996. High-pressure and high-temperature in situ x-ray diffraction study of iron to above 30 GPa using MA8-type apparatus. *Geophys. Res. Lett.* 23, 953–956.
- Haavik, C., Stølen, S., Hanfland, M., Catlow, C.R.A., 2000. Effect of defect clustering on the high-pressure behaviour of wüstite. High-pressure X-ray diffraction and lattice energy simulations. *Phys. Chem. Chem. Phys.* 2, 5333–5340.
- Heinz, D.L., Jeanloz, R., 1987. Temperature measurements in the laser-heated diamond cell, in: Manghnani, M.H., Syono, Y. (Eds.). *High-Pressure Research in Mineral Physics*. Terra Scientific Publishing, Tokyo / American Geophysical Union, Washington, pp. 113–127.
- Irfune, T., Isshiki, M., Sakamoto, S., 2005. Transmission electron microscope observation of the high-pressure form of magnesite retrieved from laser heated diamond anvil cell. *Earth Planet. Sci. Lett.* 239, 98–105.
- Ito, E., Katsura, T., Suzuki, T., 1998. Metal/silicate partitioning of Mn, Co, and Ni at high-pressures and high temperatures and implications for core formation in a deep magma ocean. In: Manghnani, M.H., Yagi, T. (Eds.), *Properties of Earth and Planetary Materials at High Pressure and Temperature*, Geophysical Monograph, vol. 101. Amer. Geophys. Union, Washington, pp. 212–215.
- Kavner, A., Duffy, T.S., 2001. Pressure–volume–temperature paths in the laser-heated diamond anvil cell. *J. Appl. Phys.* 89, 1907–1914.
- Kavner, A., Panero, W.R., 2004. Temperature gradients and evaluation of thermoelastic properties in the synchrotron-based laser-heated diamond cell. *Phys. Earth Planet. Inter.* 143–144, 527–539.
- Kegler, P., Holzeid, A., Frost, D.J., Rubie, D.C., Dohmen, R., Palme, H., 2008. New Ni and Co metal–silicate partitioning data and their relevance for an early terrestrial magma ocean. *Earth Planet. Sci. Lett.* 268, 28–40.
- Keppler, H., Rubie, D.C., 1993. Pressure-induced coordination changes of transition-metal ions in silicate melts. *Nature* 364, 54–56.
- Knacke, O., Kubaschewski, O., Hesselmann, K., 1991. *Thermochemical Properties of Inorganic Substances*, 2nd ed. Springer-Verlag, Berlin.
- Leinenweber, K., Mosenfelder, J., Diedrich, T., Soignard, E., Sharp, T.G., Tyburczy, J.A., Wang, Y., 2006. High-pressure cells for in situ multi-anvil experiments. *High Press. Res.* 26, 283–292.
- Li, J., Agee, C.B., 1996. Geochemistry of mantle–core differentiation at high pressure. *Nature* 381, 686–689.
- Li, J., Agee, C.B., 2001. The effect of pressure, temperature, oxygen fugacity and composition on partitioning of nickel and cobalt between liquid Fe–Ni–S alloy and liquid silicate: implications for the Earth's core formation. *Geochim. Cosmochim. Acta* 65, 1821–1832.
- Mao, W.L., Campbell, A.J., Prakapenka, V.B., Hemley, R.J., Mao, H.-K., 2007. Effect of iron on the properties of post-perovskite silicate. In: Hirose, K., Brodholt, J., Lay, T., Yuen, D. (Eds.), *Post-perovskite: The Last Mantle Phase Transition*. AGU Monograph Series, vol. 174. American Geophysical Union, Washington, DC, pp. 37–46.
- McCammon, C.A., Liu, L.-G., 1984. The effects of pressure and temperature on non-stoichiometric wüstite,  $\text{Fe}_x\text{O}$ : the iron-rich phase boundary. *Phys. Chem. Miner.* 10, 106–113.
- McDonough, W.F., Sun, S.-S., 1995. The composition of the Earth. *Chem. Geol.* 120, 223–253.
- Murakami, M., Hirose, K., Ono, S., Tsuchiya, T., Isshiki, M., Watanuki, T., 2004. High pressure and high temperature phase transitions of  $\text{FeO}$ . *Phys. Earth Planet. Inter.* 146, 273–282.
- Ohtani, E., Yurimoto, H., Seto, S., 1997. Element partitioning between metallic liquid, silicate liquid, and lower-mantle minerals: implications for core formation of the Earth. *Phys. Earth Planet. Inter.* 100, 97–114.
- Ricolleau, A., Fiquet, G., Addad, A., Menguy, N., Vanni, C., Perrillat, J.-P., Daniel, I., Cardon, H., Guignot, N., 2008. Analytical transmission electron microscopy study of a natural MORB sample assemblage transformed at high pressure and high temperature. *Am. Mineral.* 93, 144–153.
- Righter, K., 2003. Metal–silicate partitioning of siderophile elements and core formation in the early Earth. *Annu. Rev. Earth Planet. Sci.* 31, 135–174.
- Righter, K., Drake, M.J., Yaxley, G., 1997. Prediction of siderophile element metal–silicate partition coefficients to 20 GPa and 2800 °C: the effect of pressure, temperature,  $\text{fO}_2$  and silicate and metallic melt composition. *Phys. Earth Planet. Inter.* 100, 115–134.
- Rubie, D.C., 1999. Characterizing the sample environment in multianvil high-pressure experiments. *Phase Transitions* 68, 431–451.
- Seagle, C.T., Heinz, D.L., Campbell, A.J., Prakapenka, V.B., Wanless, S.T., 2008. Melting and thermal expansion in the Fe–FeO system at high pressure. *Earth Planet. Sci. Lett.* 265, 655–665.
- Shen, G., Mao, H.-K., Hemley, R.J., Duffy, T.S., Rivers, M.L., 1998. Melting and crystal structure of iron at high pressures. *Geophys. Res. Lett.* 25, 373–376.
- Shen, G., Rivers, M.L., Wang, Y., Sutton, S.R., 2005. Facilities for high-pressure research with the diamond anvil cell at GSECARS. *J. Synchrotron Radiat.* 12, 642–649.
- Sinmyo, R., Hirose, K., Nishio-Hamane, D., Seto, Y., Fujino, K., Sata, N., Ohishi, Y., 2008. Partitioning of iron between perovskite/postperovskite and ferropericlase in the lower mantle. *J. Geophys. Res.* 113, B11204.
- Stebbins, J.F., McMillan, P.F., Dingwell, D.B., 1995. *Structure, dynamics, and properties of silicate melts*. Reviews in Mineralogy, vol. 32. Mineralogical Society of America, Washington, DC.
- Stixrude, L., Karki, B., 2005. Structure and freezing of  $\text{MgSiO}_3$  liquid in Earth's lower mantle. *Science* 310, 297–299.
- Stølen, S., Grønvold, F., 1996. Calculation of the phase boundaries of wüstite at high pressure. *J. Geophys. Res.* 101, 11531–11540.
- Takafuji, N., Hirose, K., Mitomi, M., Bando, Y., 2005. Solubilities of O and Si in liquid iron in equilibrium with  $(\text{Mg,Fe})\text{SiO}_3$  perovskite and the light elements in the core. *Geophys. Res. Lett.* 32, L06313.
- Thibault, Y., Walter, M.J., 1995. The influence of pressure and temperature on the metal–silicate partition coefficients of nickel and cobalt in a model C1 chondrite and implications for metal segregation in a deep magma ocean. *Geochim. Cosmochim. Acta* 59, 991–1002.
- Uchida, T., Wang, Y., Rivers, M.L., Sutton, S.R., Weidner, D.J., Vaughan, M.T., Chen, J., Li, B., Secco, R.A., Rutter, M.D., Liu, H., 2002. A large-volume press facility at the Advanced Photon Source: diffraction and imaging studies on materials relevant to the cores of planetary bodies. *J. Phys. Condens. Matter* 14, 11517–11523.
- Wade, J., Wood, B.J., 2005. Core formation and the oxidation state of the Earth. *Earth Planet. Sci. Lett.* 236, 78–95.
- Walter, M.J., Newsom, H.E., Ertel, W., Holzheid, A., 2000. Siderophile elements in the Earth and Moon: metal/silicate partitioning and implications for core formation. In: Canup, R.M., Righter, K. (Eds.), *Origin of the Earth and Moon*. Univ. of Arizona, Tucson, pp. 265–290.
- Williams, Q., Jeanloz, R., 1988. Spectroscopic evidence for pressure-induced coordination changes in silicate glasses and melts. *Science* 239, 902–905.
- Zhang, F., Oganov, A.R., 2006. Valence state and spin transitions of iron in Earth's mantle silicates. *Earth Planet. Sci. Lett.* 249, 436–444.